IEEE Access
Multidisciplinary | Rapid Review | Open Access Journal

Received September 10, 2019, accepted September 16, 2019, date of publication September 19, 2019,
date of current version October 2, 2019.

Digital Object Identifier 10.1109/ACCESS.2019.2942482

Operation Principle and Torque Component Quantification of Short-Pitched Flux-Bidirectional-Modulation Machine

SHUANGXIA NIU[1], (Senior Member, IEEE), TIANTIAN SHENG[1], XING ZHAO[1], AND XIAODONG ZHANG[2]

[1]Department of Electrical Engineering, The Hong Kong Polytechnic University, Hong Kong
[2]Shenzhen In Drive Amperex Company Ltd., Shenzhen 518052, China

Corresponding author: Xiaodong Zhang (xiaodong@eee.hku.hk)

This work was supported by the Research Grant Council of the Hong Kong Government under Project PolyU 15250916/16E.

ABSTRACT This paper analyzes the operation principle of a short-pitched flux-bidirectional-modulation machine, with especial efforts in terms of its torque component quantification and back EMF harmonics reduction. With the bidirectional-flux-modulation effect, increased equivalent permeance of the air gap is constructed to enhance the machine torque production. Meanwhile, with the shorted-pitched distributed winding design, the electrical gear ratio of machine is increased to realize boosted torque production, and a variety of back-EMF harmonics are eliminated, thus the torque ripple is reduced. In this paper, the machine operation principle is analyzed based on a simple magnetomotive force-permeance analytical model. The torque components and back EMF harmonics are deduced by winding factor analysis. It is revealed that in the proposed machine, the excitation fields with pole pairs of 2, 22 and 46 have generated the effective back-EMF and constant torque and their contribution percentages are 77%, 20% and 3% respectively. Rotor-PM and stator-PM contribute 59% and 41% of the torque respectively. With the 5/6 short-pitch design, the 3rd, 5th and 7th back-EMF harmonics are reduced by 55%, 88% and 88% respectively and the THD of back-EMF is reduced 56.8%. A prototype is fabricated and tested for experimental verification.

INDEX TERMS Bidirectional-flux modulation, permanent magnet, short pitch.

I. INTRODUCTION

With the development of integrated-circuit and artificial intelligence, robotic technology grows rapidly in recent years [1], [2]. As the key actuator, electric machines play a crucial role in operation of the robotic system. Different from the conventional applications, robotic systems usually operate at extremely low speed and with high torque density. Nowadays, most of the robotic systems apply the relative high speed machines together with the large-scale mechanical reducers, such as the RV and harmonic reducers to increase torque production [3], [4]. However, the mechanical reducers would increase the volume and weight of the system, satisfy the system efficiency and reduce the reliability of system. It is desirable to find high-torque-density direct-drive machines to improve the efficiency and reliability.

The associate editor coordinating the review of this manuscript and approving it for publication was Xiaodong Sun.

Currently, fractional-slot concentrate-winding permanent magnet (PM) synchronous machines are invested for direct-drive propulsion. These machines may be designed with more pole pairs than distributed-winding PMSMs with the same slot number, as their slot per pole per phase q is less than 1 [5]. However, for conventional fractional slot concentrate-winding machine, the number of slots is usually designed as approximately twice of the PM pole pairs [6]. Within the fixed outer diameters, with the increasing of the slot number, the slot filling factor will be reduced consequently, since the insulating materials and the slot wedges take up increased proportion of slot area. The reduced slot filling factor thus affects the torque density, which is undesired for robotic system.

Fortunately, flux modulation machines (FMMs), can decouple the relationship of the winding and PM pole pairs, and with the modulation of stator teeth, the pole pair number of stator winding could be designed very low and hence reducing the slot number and improving the slot filling factor.

Flux modulation machine operates on the principle that a small displacement of the rotor will produces a large displacement of the axes of the maximum and minimum permeance, which is stated as gear effect [7]. Sometimes FMMs are also named as magnetic geared machine and Vernier machine.

Basically, FMMs could be divided into two categories, the electric excitation FMMs and PM excited FMMs. Flux-modulation reluctance machine and DC excitation flux-modulation machine belong to electric excitation FMMs [7]–[11]. In flux-modulation reluctance machine, the winding generates both excitation and armature fields, and the variation of the permeance is used to produce effective reluctance torque [7], [8]. In DC excitation flux-modulation machines, the excitation field is modulated to couple with the armature field to generate torque [10], [11]. PM excited FMMs can usually divided as Rotor-PM FMMs, Stator-PM FMMs. Rotor-PM flux-modulation machine is firstly studied in [12]. It is interesting to see that Rotor-PM FMMs have the similar machine structure with the conventional PMSMs, except the combination of the winding and PM poles. Compared with PMSMs, rotor-PM FMMs have increased torque performance [13]–[18]. Stator-PM Vernier machines have robust rotor structure with PMs in stator, so the heat dissipation could be improved, which are very suitable to be designed as linear motor due to the cost of the no-PM long track could be reduced significantly [19]–[21]. Dual-PM excited FMMs is a new class of FMMs [22]–[26]. FMMs with closed-slot or split-teeth structure are developed [24], [25]. However, some important essential issues the effect of the parallel magnetic path and the torque/back-EMF percentages contributed by the excitation field harmonics of such machine have not been fully revealed in these literatures.

In this paper, one novel dual-PM FMMs with bidirectional flux modulation and short-pitched distributed windings and parallel magnetic path is investigated. The operation principle is introduced and the prototype is tested. The advantages of the parallel magnetic path, distributed windings and short-pitched coils are discussed in paper.

II. MACHINE CONFIGURATION

A. MACHINE STRUCTURE

Fig. 1 shows the topology of the proposed machine, which has 24 slots, 22 rotor pole pairs and 2 winding pole pairs. The reason to use a 24-stator-slot and 22-rotor-pole-pair design is based on the considerations of high magnetic gearing ratio as well as zero unbalanced magnetic pull. The PMs installed in the stator/rotor slot openings are magnetized with the same radially outward direction. Fig. 2 shows the short-pitched distributed windings, in which the 5/6 short-pitched coils is artificially applied to eliminate 3rd, 5th and 7th back-EMF harmonics to reduce torque ripple. The effectiveness of this design will be explained in section III.

B. DESIGN PARAMETERS

Fig. 3 illustrates the key dimensions of the proposed machine. To obtain the maximum torque, the key dimensions such as

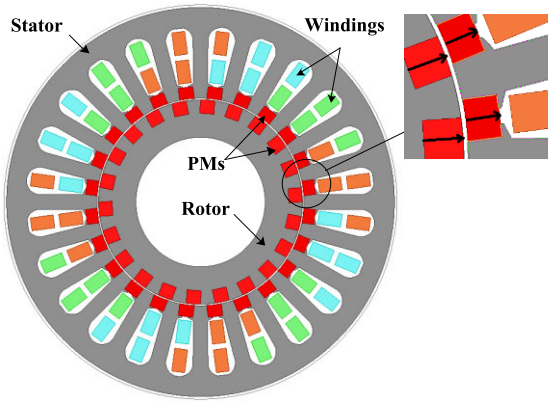

FIGURE 1. Topology of the proposed dual-PM FMM.

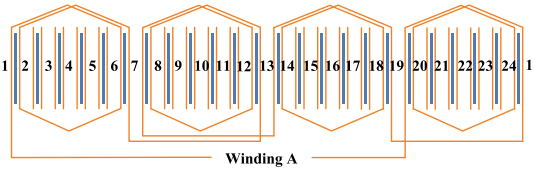

FIGURE 2. Winding distribution of the proposed dual-PM FMM.

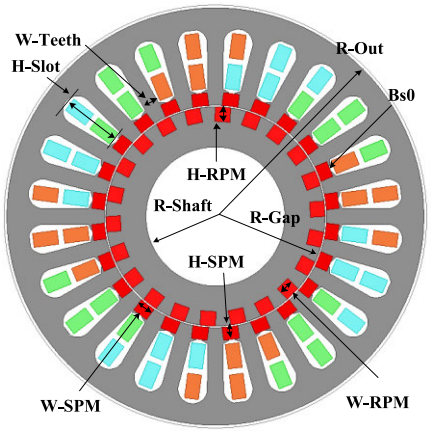

FIGURE 3. Key dimensions of the machine of the proposed machine.

W-SPM, H-SPM, W-RPM and H-RPM shown in Fig. 3 are optimized by using the genetic algorithm. The optimized dimensions and some key design parameters are given in Table 1 and 2.

III. OPERATION PRINCIPLE AND ELELCTROMAGNETIC PERFORMANCE

A. OPERATION PRINCIPLE

1) FLUX BIDIRECTIONAL MODULATION AND FIELD COMPONENTS ANALYSIS

This proposed dual-PM FMM can be regarded as an integration of one rotor-PM FMM and one stator-PM FMM with a symmetrical flux modulation. The rotor-PM machine has the rotor with 22 teeth and 22 pieces of PMs and the stator with 24-slot 2-pole-pair windings, as shown in Fig. 4. The stator-

TABLE 1. Key dimensions of the proposed dual-PM FMMs.

Items	Value	Items	Value
R-Out (mm)	60	H-Slot (mm)	18
Axial Length (mm)	55	W-SPM (mm)	4.4
Air Gap (mm)	0.5	H-SPM (mm)	4.1
R-Gap (mm)	31.75	W-RPM (mm)	4.4
R-Shaft (mm)	20	H-RPM (mm)	3.7
W-Teeth(mm)	4.6	Bs0 (mm)	1.7

TABLE 2. Key design parameters of the proposed dual-PM excited vernier machine.

Items	Value	Items	Value
Rated speed (rpm)	200	Number of turns	25
Rated torque (Nm)	21.5	Coil space factor	0.7
Rated voltage (V)	40	Current density A/(mm)^2	4.2
Rated current (RMS)	7		
Rated Power (W)	450	Heat dissipation condition	Nature ventilation

PM machine has the same rotor design except removed PMs and the same stator with 24 pieces of PM installed in the slot openings, as shown in Fig. 5. The excitation fields produced by the rotor-PM or the stator-PM have the same pole pairs and the same rotational velocity and the magnetic path is parallel with each other, so the bidirectional flux modulation effect due to the parallel magnetic path with these two machines can be combined together. Therefore, figuring out the characteristics of the excitation field components produced by rotor PMs and stator PMs is the key to reveal the working principle of this proposed machine.

Fig. 4 shows the simulation results of the rotor-PM excitation fields, in which Fig. 4(a) shows the field distribution and Fig. 4(b) gives the waveform of the radial magnetic intensity along air-gap. To figure out the pole pairs of the excitation fields, the FFT analysis of the radial magnetic intensity is conducted and shown in Fig. 4(c).

Ignoring the harmonics with the amplitude of less than 0.1 T, it is found that rotor-PM excitation fields have the components with the order of 22^{nd}, 66^{th}, 110^{th}, 154^{th}, 2^{nd} and 46^{th} harmonics. Since the fundamental harmonic of the FFT analysis is along the circumference of the air-gap, the harmonic orders here represent the pole pairs of the excitation field components. The velocities of these field components are also figured out.

According to the magnetic field modulation theory, the pole pair P_{ER} and the rotational velocity of the excitation field components ω_{ER} are expressed as.

$$\begin{cases} P_{ER} = |uP_{PMR} + vN_S| \\ \omega_{ER} = \dfrac{uP_{PMR}}{uP_{PMR} + vN_S}\omega_m + \dfrac{vN_S}{uP_{PMR} + vN_S}\omega_{Ns} \\ u = 1, 3, 5 \ldots v = 0, \pm 1, \pm 2.. \end{cases} \quad (1)$$

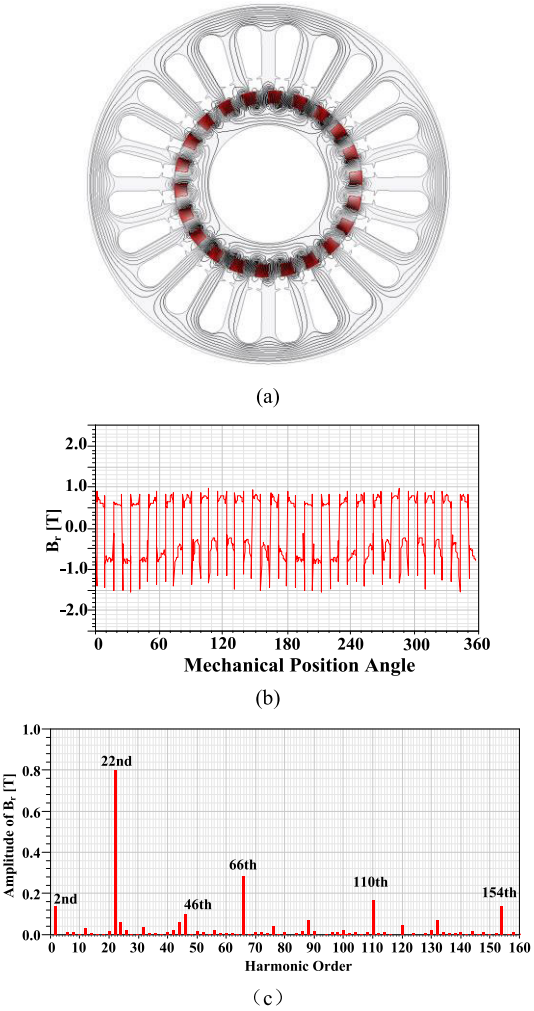

FIGURE 4. Rotor-PM excitation field. (a) Field distribution. (b) Radial magnetic intensity along air-gap. (c) FFT analysis of the rotor-PM excitation field intensity.

TABLE 3. Pole pairs, intensity, and velocity of the rotor-PM excitation field.

P_{ER}	(u,v)	B_{ER} (T)	ω_{ER}	P_{ER}	(u,v)	B_{ER} (T)	ω_{ER}
2	(1,-1)	0.14	$-11\omega_m$	66	(3,0)	0.28	ω_m
22	(1,0)	0.8	ω_m	110	(5,0)	0.16	ω_m
46	(1,1)	0.10	$11\omega_m/23$	154	(7,0)	0.15	ω_m

where P_{PMR} is the pole pair number of rotor-PM, N_S is the stator teeth number, ω_m is the mechanical rotational velocity of rotor and ω_{NS} is the rotational velocity of the stator teeth.

With the data in Fig. 4(c), the pole pair, magnetic intensity and velocity of the field components can be figured out, which are listed in Table 3. The magnetic intensity and velocity determine the back-EMF generating capability simultaneously, so the velocity of the fields should be found. It is found that the velocity of the field with 2 pole pairs is -11 times of ω_m, the fields with 22, 66, 110, 154 pole pairs have same velocity with ω_m and the velocity of field with 46 pole pairs is 11/23 of ω_m.

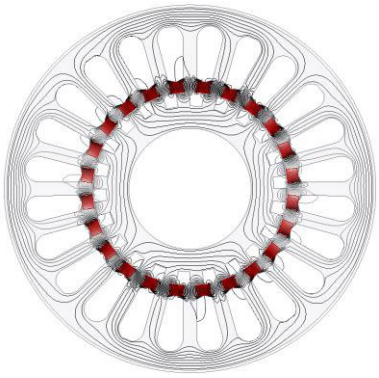

(a)

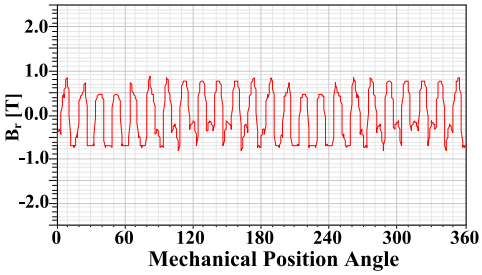

(b)

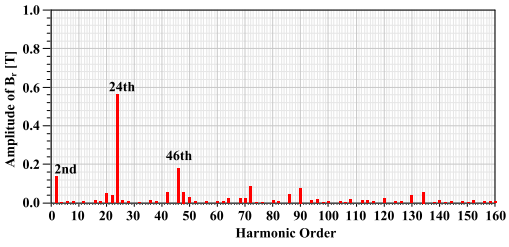

(c)

FIGURE 5. Stator-PM excitation field. (a) Field distribution. (b) Radial magnetic intensity along air-gap. (c) FFT analysis of the rotor-PM excitation field intensity.

The stator-PM generated fields are also analyzed in the similar way. Fig. 5(a) shows the field distribution, Fig. 5(b) presents the waveform of the radial magnetic intensity along air-gap and Fig. 5(c) shows the corresponding FFT analysis of the waveform. Ignoring the harmonics with amplitude of less than 0.1 T, it is observed that the main components in stator-PM generated fields have the pole pair number of 2, 24 and 46. By using field modulation theory, the pole pair P_{ES} and velocity ω_{ES} of the fields produced by stator-PM can be expressed as:

$$\begin{cases} P_{ES} = |mP_{PMS} + nN_R| \\ \omega_{ES} = \dfrac{mP_{PMS}}{mP_{PMS} + nN_R}\omega_{PM} + \dfrac{nN_R}{mP_{PMS} + nN_R}\omega_m, \\ m = 1, 3, 5 \ldots n = 0, \pm 1, \pm 2 \ldots \end{cases} \quad (2)$$

TABLE 4. Pole pairs, intensity, and velocity of the stator-PM excitation field.

P_{ES}	(m,n)	B_{ES} (T)	ω_{ES}
2	(1,-1)	0.14	$-11\omega_m$
24	(1,0)	0.56	0
46	(1,1)	0.18	$11\omega_m/23$

where P_{PMS} is the pole pair number of stator-PMs, N_R is the rotor teeth and ω_{PM} is the velocity of the stator-PMs. Noticeably, the PMs here are stationary and modulators are the rotor teeth, while in (1), the PMs are rotary and modulators are the stator teeth.

Similarly, combining with the data in Fig. 5(c), the pole pair number, magnetic intensity and velocities of the stator-PM excitation fields can be figured out. The corresponding data are listed in Table 4.

It is found that for the stator-PM excitation fields, the component with 2 pole pairs also has the velocity of $-11\omega_m$ and the component with 46 pole pairs with $11/23\omega_m$, exactly the same with the situation in the rotor-PM machine. Since the dominant field components produced by the rotor-PM and stator-PM have the same pole pair and the same velocity, it is reasonable to integrate these two machines together to intensify the field to increase the effective torque. This reveals the basic working principle of the proposed dual-PM PMM.

The final excitation field produced by both stator-PM and rotor-PM has also been analyzed and presented to verify the previous analysis. Fig. 6(a) presents the field distribution of the dual-PM excitation field, Fig. 6(b) gives the waveform of radial magnetic intensity along air-gap and Fig. 6(c) shows the FFT analysis of the dual-PM excitation filed intensity.

Similarly, ignoring the harmonics with amplitude of less than 0.1 T, there are mainly seven components of the dual-PM excitation fields. Based on the above analysis, it is known that the 2^{nd} and 46^{th} order harmonics are produced by both rotor PMs and stator PMs, the 24^{th} order harmonic is produced by stator PMs and the 22^{nd}, 66^{th}, 110^{th}, 154^{th} order harmonics are produced by rotor PMs. It is found that 2^{nd} harmonic has the maximum product of magnetic intensity and velocity, so it will be the dominant effective excitation field component.

The field distributions produced by dual-PM at different rotor positions are presented in Fig. 7 to further explain the working principle. It is observed that there is the field with 2 pole pairs in the stator area. From Fig. 7(a) to Fig. 7(d), the rotor moves 12.27° degrees while the *d-axis* of the rotor moves −135° degrees. The velocity of the field with 2 pole pairs is −11 times of rotor speed ω_m, which verified the theory analysis.

It is found that in this dual-PM excited Vernier machine, the excitation field has much more harmonics. While, it is known that in conventional PMSMs, the high order harmonics would cause back-EMF distortion and torque ripple. So the influences to back-EMF of FMM should be figured out in the dual-PM FMM.

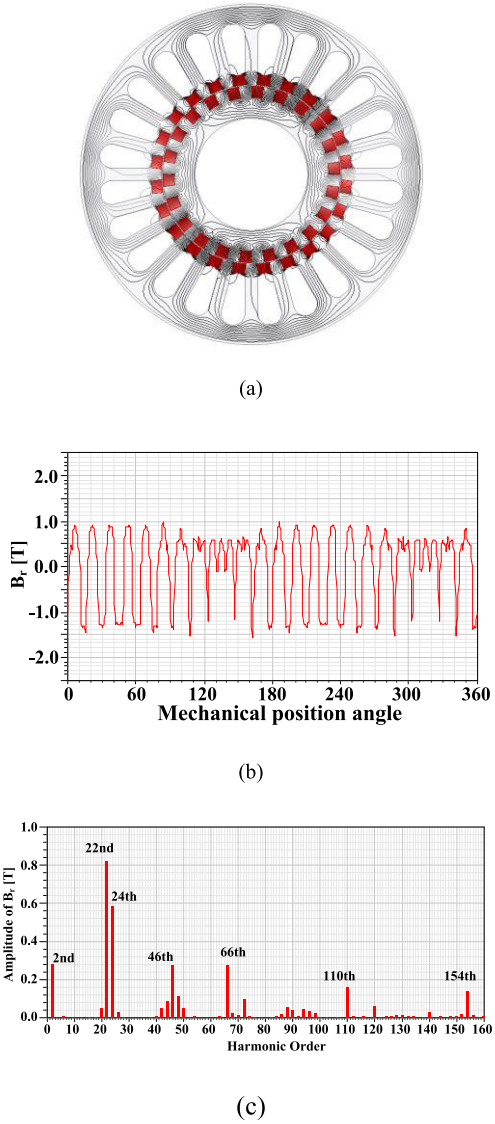

FIGURE 6. Dual-PM excitation field. (a) Field distribution. (b) Radial magnetic intensity along air-gap. (c) FFT analysis of the rotor-PM excitation field intensity.

2) WINDING FACTORS

To analyze the influence of excitation harmonics to the back-EMF of the proposed FMM, the winding factors for each harmonic should be figured out. According to the winding theory, the pole pitch τ, slot-pitch angle α, slots per pole per phase q and coil-pitch y_1 can be calculated by:

$$\begin{cases} \tau = \dfrac{Z_S}{2P_W} = 6 \\ \alpha = \dfrac{2\pi P_W}{Z_S} = \dfrac{\pi}{6} \\ q = \dfrac{Z_S}{2mP_W} = 2 \\ y_1 = 5 \end{cases} \tag{3}$$

where P_W is the winding pole pair number.

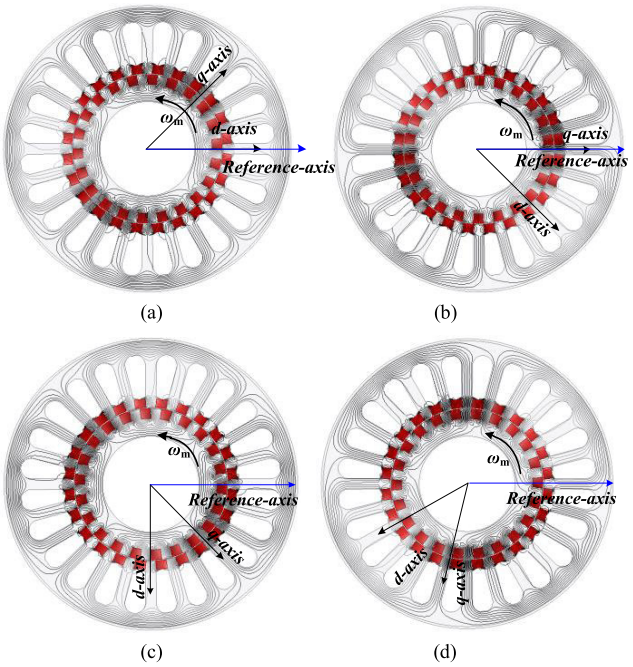

FIGURE 7. Excitation flux distribution of the proposed dual-PM FMM with rotor at different mechanical positions. (a) 0°. (b) 4.09°. (c) 8.18 °. (d) 12.27°.

TABLE 5. Coil-pitch factor, winding distribution factor, and winding factor for main excitation field components.

P_E	k_y	k_q	k_W	P_E	k_y	k_q	k_W
2	0.97	0.97	0.93	66	-0.71	-0.71	0.5
22	0.97	-0.97	-0.93	110	0.26	-0.26	-0.07
24	0	-1	0	154	0.26	0.26	0.07
46	-0.97	0.97	-0.93				

The coil-pitch factor k_{yPE}, winding distribution factor k_{qPE}, and winding factor k_{wPE} for the field components with P_E pole pairs can be expressed as:

$$\begin{cases} k_{yP_E} = \sin(\dfrac{y_1}{\tau}\dfrac{\pi}{2}\dfrac{P_E}{P_W}) \\ k_{qP_E} = \dfrac{\sin(\frac{q\alpha}{2}\frac{P_E}{P_W})}{q\sin(\frac{\alpha}{2}\frac{P_E}{P_W})} \\ k_{WP_E} = k_{yP_E}k_{qP_E} \end{cases} \tag{4}$$

where P_E is the pole pair number of the excitation field component.

The calculated results of coil-pitch factor, winding distribution factor and winding factor for the main excitation field components are shown in Table 5.

3) BACK-EMF AND TORQUE

The back-EMF e_{PE} produced by the excitation field component with P_E pole pair number can be calculated by:

$$e_{P_E} = lr_gNk_{WP_E}B_E\,|\omega_E|\sin(P_E\omega_E t) \tag{5}$$

where l is the axial length of the machine, r_g is the air-gap radius, N is the conductor number, B_E and ω_E is the magnetic

TABLE 6. Amplitude and velocity of the key back-EMF components.

P_E	*Back-EMF*		P_E	*Back-EMF*	
	A_E (p.u)	$P_E\omega_E$		A_E	$P_E\omega_E$
2	1.0	$-22\omega_m$	66	0.05	$66\omega_m$
22	-0.26	$22\omega_m$	110	-0.003	$110\omega_m$
24	0	0	154	0.003	$154\omega_m$
46	-0.04	$22\omega_m$			

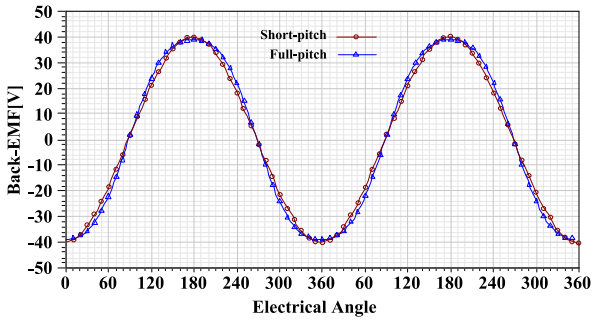

FIGURE 8. Simulation result of the Back-EMF for short-pitched and full-pitched coils in dual-PM FMM.

intensity and velocity of this field component. Noticeably, B_E is produced by both of the rotor-PM and stator-PM, which is the sum of B_{ER} and B_{ES}.

Taking the data in Table 3, 4 and 5 into (5), the back-EMF components caused by the corresponding excitation field components can be calculated and the results are listed in Table 6. Using the standard unitary expression, the amplitudes of each back-EMF component A_E are written as the percentage of maximum value.

The back-EMF for Phase A could be expressed by:

$$e_A = \sum_{i=1}^{7} A_E \sin(P_E \omega_E t) \tag{6}$$

According to the data in Table 6 and Eq. (6), it is found that the fundamental harmonic of the back-EMF has the velocity of $22\omega_m$. The excitation fields with 2, 22 and 46 pole pairs have a positive contribution to the fundamental harmonic and they account for 77%, 20% and 3% of the total back-EMF respectively. The excitation field with 24 pole pairs has no influence on the back-EMF due to either of the zero winding factor or the zero rotational velocity. The field components with 66, 110 and 154 pole pairs produce the 3rd, 5th and 7th order harmonics of the back-EMF.

By further analysis, it is found that the 3rd, 5th and 7th harmonic account for 3.8%, 0.2% and 0.2% of the fundamental harmonic one. The THD of the back-EMF waveform is 3.8%. This is contributed by the short pitched coil design. If the full pitch winding is used, which means y_1 equal 6 in (5), the 3nd, 5th and 7th harmonics will account 8.5%, 1.7% and 1.7% respectively and the THD will reach 8.8%. This results can explain why the 5/6 short-pitched winding is used for this dual-PM excited Vernier machine.

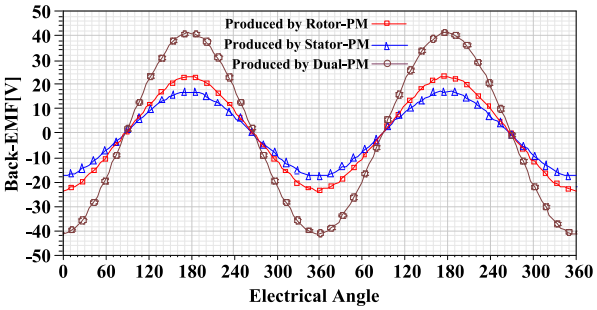

FIGURE 9. Simulation result of the Back-EMF produced by rotor-PM, stator-PM, and dual-PM vernier.

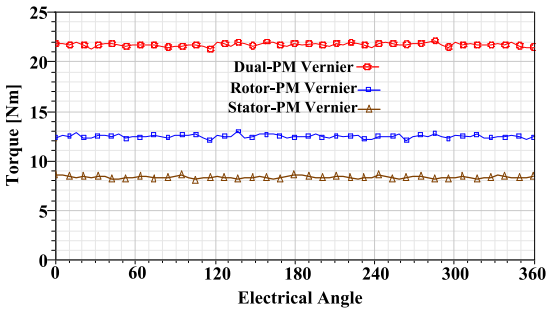

FIGURE 10. Simulation result of the torque of the rotor-PM, stator-PM, and dual-PM FMM.

The simulation results of back-EMF waveforms for this machine by using short-pitched coils and full-pitched coils are presented and compared in Fig. 8 to verify the theoretical analysis. It is found that for the full-pitch machine, the crest and trough of the waveform appears flat, which is caused mainly by the low older odd harmonics, namely the 3rd, 5th and 7th harmonics, while for the short-pitch machine, the back-EMF is better sinusoidal waveform.

With the data in Table 3 and 4, the contribution of the rotor-PM and stator-PM to the final back-EMF could also be figured out. It is found that rotor-PM and stator-PM contributes 59% and 41% of the final back-EMF, respectively. Rotor-PM has 18% higher contribution than the stator-PM, which is mainly caused by the field component with the 22 pole pairs. This component only exists in the rotor-PM machine but not in the stator-PM machine. To verify the analysis, the simulations based on finite-element method are conducted. Fig. 9 shows the phase back-EMF waveforms for rotor-PM excitation machine, stator-PM excitation machine and dual-PM excitation machine. It is found that the back-EMF amplitudes of rotor-PM excitation, stator-PM excitation and dual-PM excitation machines are 24 V, 17 V and 41 V respectively. The rotor-PM and stator-PM contributes 60% and 40% respectively to the final back-EMF, which agrees well with theory analysis.

The torque contributed by the rotor-PM, stator-PM and dual-PM is also analyzed. It is found in Fig. 10 that with only rotor-PM excitation, the average torque is 12.75 Nm, with only stator-PM excitation, the average torque is 8.8 Nm and

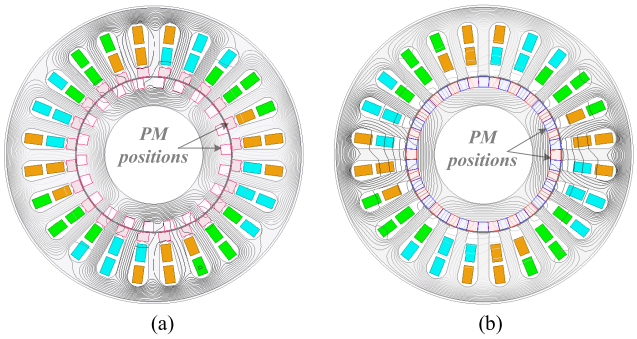

FIGURE 11. Armature magnetic field distribution. (a) The proposed dual-PM FMM. (b) Rotor-PM FMM.

with dual-PM excitation, the average torque is 21.5 Nm. The rotor-PM and stator-PM contribute about 60% and 40% of the total torque, which agrees with the theoretical analysis well.

In addition, since the back-EMF waveform in Fig. 10 has good sinusoidal waveform due to the 5/6 short-pitch winding design, the torque ripple of the dual-PM FMM is small. It is observed that the peak-peak value of torque ripple is only about 0.8 Nm, accounting for only 3.7% of the rated torque.

It is worth mentioning that the main objective of this paper is to investigate the influence of PM arrangement as well as armature winding design on harmonics distribution, while the influence of machine structure parameters is not considered [27]–[30] but will be included in future works.

B. PARALLEL MAGNETIC PATH

Parallel magnetic path is the major characteristic of this dual-PM FMM. Due to the parallel magnetic path, the average permeability of the magnetic path is significantly improved. Consequently, under the same MMF, the proposed machine could get stronger field in the air-gap, so the torque could be improved.

To demonstrate the armature field strengthening effect of the parallel magnetic path characteristic, the armature magnetic field of the proposed dual-PM FMM and the conventional rotor-PM Vernier machine are simulated and compared in Fig. 11, where the material of PMs is assigned as vacuum to remove the influence of excitation MMF. The rotor-PM Vernier machine has 22 pole pairs of PM in rotor and 2 pole pairs of windings. The key dimensions for these two machines remain the same.

It is observed that for the dual-PM FMM, the armature field goes through stator teeth, air-gap and rotor-teeth to form the loop, without passing the PMs, while for the conventional rotor-PM FMM, the armature filed has to pass the PMs to form the loop. Since the permeability of the PMs is as small as vacuum, so under same MMF, the air-gap flux density of dual-PM FMM could be much stronger than conventional rotor-PM FMM.

Fig. 12 shows the simulation results of the armature magnetic field intensity along air gap for the proposed

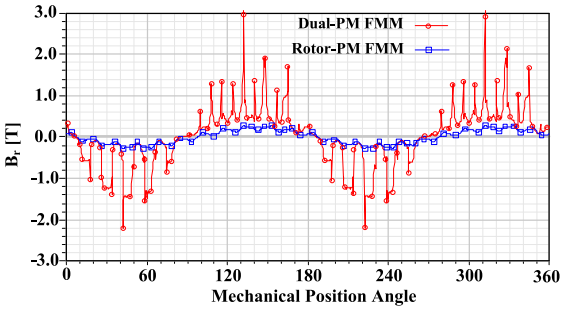

FIGURE 12. Radial armature magnetic field intensity along air-gap of the proposed dual-PM FMM and rotor-PM FMM.

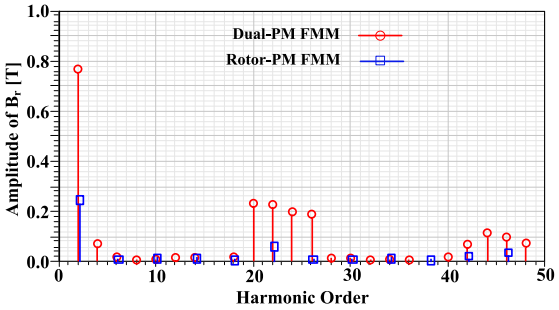

FIGURE 13. FFT analysis of the armature magnetic field intensity in air gap for the proposed dual-PM FMM and rotor-PM FMM.

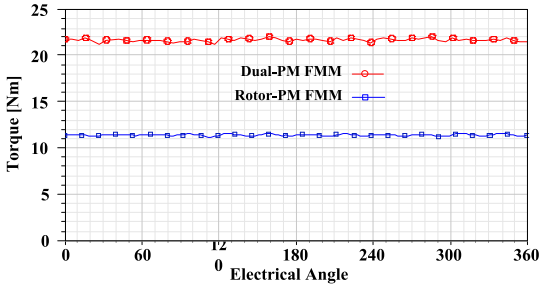

FIGURE 14. Simulation results of torque for the proposed dual-PM excited Vernier machine and rotor-PM Vernier machine.

dual-PM FMM and the conventional rotor-PM FMM, and Fig. 13 presents the FFT analysis of the waveforms.

It is observed that under the same MMF, for the dominant effective harmonic component with the pole pair number of 2, the amplitude for dual-PM and conventional FMM is 0.76 T and 0.24 T respectively. The parallel magnetic path generates much stronger field intensity under same MMF. From the other perspective, the half-closed slot structure for rotor and stator in the proposed machine actually increases the average permeance of the air-gap, which is equivalent to reduce the air-gap. Consequently, the magnetic intensity and the torque of the proposed machine could be improved.

To verify the advantage of the proposed dual-PM FMM over conventional rotor-PM FMM, Fig. 14 gives the simulation results of the torque for them. It is found that the average torque for the proposed machine and conventional machine is 21.5 Nm and 11.5 Nm respectively. The torque

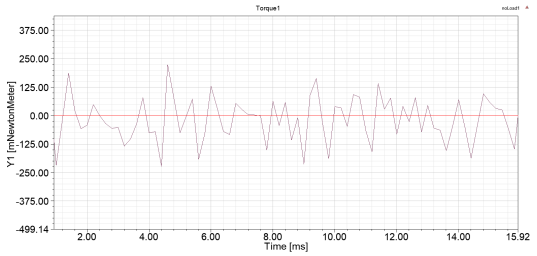

FIGURE 15. Cogging torque of the machine.

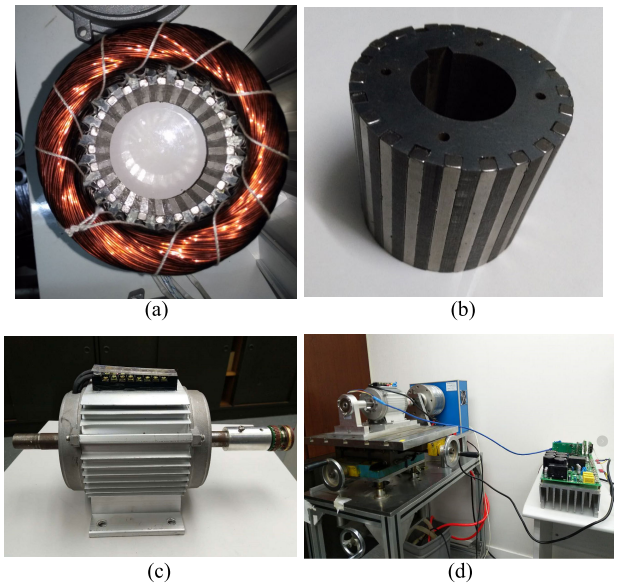

FIGURE 16. The prototype and testing bed. (a) Stator. (b) Rotor. (c) Appearance of the prototype. (d) Testing system.

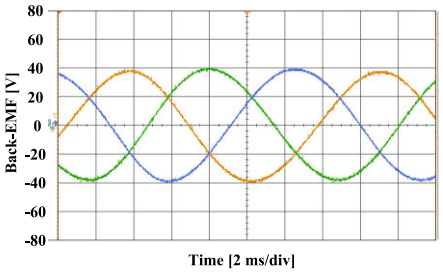

FIGURE 17. Measured three-phase back-EMF waveforms.

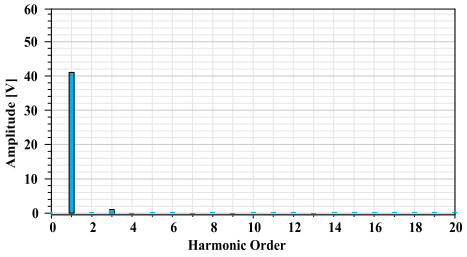

FIGURE 18. FFT analysis of one phase back-EMF waveform.

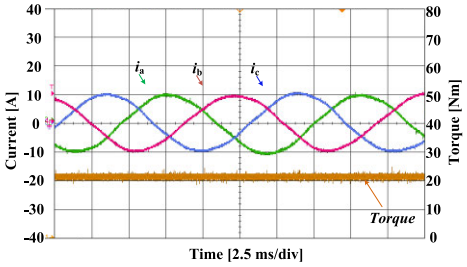

FIGURE 19. Measured phase current and torque waveforms.

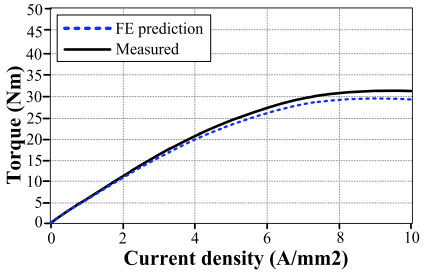

FIGURE 20. Torque ability test.

density for the proposed machine is about 1.87 times of the conventional FMM. It is well known that in PM machine the slots/pole combination plays the main role in deciding the cogging torque amplitude [26]. The increasing frequency of the cogging torque could effectively reduce the amplitude of cogging torque oscillation. The it is desired to get a slot/pole combination with the higher least common multiple. Therefore, we select 24/22 slot/pole design to reduce the cogging torque. As shown in Fig. 15, the cogging torque of the proposed machine is very small.

IV. EXPERIMENTAL VERIFICATION

To verify the performance of the dual-PM FMM, the prototype has been built and tested. The data in terms of back-EMF, torque and efficiency have been tested. Fig. 16 gives the pictures of the stator, rotor, prototype appearance and testing system. The steel lamination material is B50A470-A and PM material is NdFeB-N38EH. One aluminum shell with fins is used to package stator and rotor.

Fig. 17 shows the no-load back-EMF waveforms when the prototype operates at rated 200 rpm. It is seen that the measured back-EMF has good sinusoidal waveform. To find out the THD of the waveform, the FFT analysis is conducted based on the measured data and the result is shown in Fig. 18. It is seen that the 3rd harmonic has the amplitude of 1.5 V, accounting 3.6 % of the fundamental harmonic. The 5th and 7th harmonics have the neglectable influence contributed by the short-pitch design. The total THD for the measured back-EMF is about 3.6%, which agrees well with the analysis.

Fig. 19 shows the driving current and measured torque. The current is a sinusoidal waveform with 10 A amplitude and the measured torque is about 21.5 Nm. The average torque value agrees well with simulation analysis. Fig. 20 shows the tested

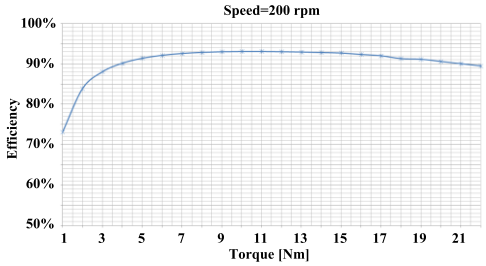

FIGURE 21. Measured efficiency under rated speed.

torque ability. It can be seen the tested result also agree with simulation result, and the maximum torque can reach 31 Nm approximately. Fig. 21 gives the measured efficiency under various torque and rated speed. It is seen that the average efficiency is about 90% in total torque range.

V. CONCLUSION

Aiming for direct robotic applications, a dual-PM FMM with shorted-pitched winding is investigated in this paper. It is shown that for the proposed machine, the excitation fields with pole pairs of 2, 22 and 46 have generated the effective back-EMF and constant torque and their contribution percentages are 77%, 20% and 3% respectively. Rotor-PM and stator-PM contribute 59% and 41% of the torque respectively. With the 5/6 short-pitch design, the 3rd, 5th and 7th back-EMF harmonics are reduced by 55%, 88% and 88% respectively and the THD of back-EMF is reduced 56.8%. Compared with the conventional FMM, the torque of the proposed one is improved by 87% with dual-PM and parallel magnetic path design. This machine has great potential in robotic applications due to its torque density, low-speed characteristic and high efficiency.

REFERENCES

[1] J. Guo, T. Bamber, Y. Zhao, M. Chamberlain, L. Justham, and M. Jackson, "Toward adaptive and intelligent electroadhesives for robotic material handling," *IEEE Robot. Autom. Lett.*, vol. 2, no. 2, pp. 538–545, Apr. 2017.
[2] Y. Zhang, J. Xiao, and W. He, "Dynamical formulation and analysis of RV reducer," in *Proc. Int. Conf. Eng. Comput.*, Hong Kong, China, May 2009, pp. 201–204.
[3] C.-H. Han, C.-C. Wang, and M. Tomizuka, "Suppression of vibration due to transmission error of harmonic drives using peak filter with acceleration feedback," in *Proc. 10th IEEE Int. Workshop Adv. Motion Control*, Trento, Italy, Mar. 2008, pp. 182–187.
[4] A. M. El-Refaie, "Fractional-slot concentrated-windings synchronous permanent magnet machines: Opportunities and challenges," *IEEE Trans. Ind. Electron.*, vol. 57, no. 1, pp. 107–121, Jan. 2010.
[5] W. Fei and P. C.-K. Luk, "Torque ripple reduction of a direct-drive permanent-magnet synchronous machine by material-efficient axial pole pairing," *IEEE Trans. Ind. Electron.*, vol. 59, no. 6, pp. 2601–2611, Jun. 2012.
[6] C. H. Lee, "Vernier Motor and Its Design," *IEEE Trans. Power App. Syst.*, vol. PAS-82, no. 66, pp. 343–349, Jun. 1963.
[7] K. C. Mukherji and A. Tustin, "Vernier reluctance motor," *Proc. Inst. Electr. Eng.*, vol. 121, no. 9, pp. 965–974, Sep. 1974.
[8] X. Zhao and S. Niu, "Design and optimization of a novel slot-PM-assisted variable flux reluctance generator for hybrid electric vehicles," *IEEE Trans. Energy Convers.*, vol. 33, no. 4, pp. 2102–2111, Dec. 2018.
[9] S. Jia, R. Qu, J. Li, and D. Li, "Principles of stator DC winding excited Vernier reluctance machines," *IEEE Trans. Energy Convers.*, vol. 31, no. 3, pp. 935–946, Sep. 2016.
[10] X. Zhao, S. Niu, and W. Fu, "A novel Vernier reluctance machine excited by slot PMs and zero-sequence current for electric vehicle," *IEEE Trans. Magn.*, vol. 55, no. 6, Jun. 2019, Art. no. 8102405.
[11] X. Zhao and S. Niu, "A new slot-PM Vernier reluctance machine with enhanced zero sequence current excitation for electric vehicle propulsion," *IEEE Trans. Ind. Electron.*, to be published.
[12] A. Toba and T. A. Lipo, "Generic torque-maximizing design methodology of permanent magnet Vernier machine," in *Proc. Int. Conf. Electr. Mach. Drives Conf.*, Seattle, WA, USA, May 1999, pp. 522–524.
[13] S. L. Ho, S. Niu, and W. N. Fu, "Design and comparison of Vernier permanent magnet machines," *IEEE Trans. Magn.*, vol. 47, no. 10, pp. 3280–3283, Oct. 2011.
[14] D. Jang and J. Chang, "Effects of flux modulation poles on the radial magnetic forces in surface-mounted permanent-magnet Vernier machines," *IEEE Trans. Magn.*, vol. 53, no. 6, Jun. 2017, Art. no. 8202704.
[15] Y. Chen, W. Fu, and X. Weng, "A concept of general flux-modulated electric machines based on a unified theory and its application to developing a novel doubly-fed dual-stator motor," *IEEE Trans. Ind. Electron.*, vol. 64, no. 12, pp. 9914–9923, Dec. 2017.
[16] S. Niu, S. L. Ho, and W. N. Fu, "A novel direct-drive dual-structure permanent magnet machine," *IEEE Trans. Magn.*, vol. 46, no. 6, pp. 2036–2039, Jun. 2010.
[17] S.-U. Chung, J.-W. Kim, B.-C. Woo, D.-K. Hong, J.-Y. Lee, and D.-H. Koo, "A novel design of modular three-phase permanent magnet Vernier machine with consequent pole rotor," *IEEE Trans. Magn.*, vol. 47, no. 10, pp. 4215–4218, Oct. 2011.
[18] D. Li, R. Qu, J. Li, and W. Xu, "Consequent-pole toroidal-winding outer-rotor Vernier permanent-magnet machines," *IEEE Trans. Ind. Appl.*, vol. 51, no. 6, pp. 4470–4481, Nov./Dec. 2015.
[19] X. Zhao and S. Niu, "Design and optimization of a new magnetic-geared pole-changing hybrid excitation machine," *IEEE Trans. Ind. Electron.*, vol. 64, no. 12, pp. 9943–9952, Dec. 2017.
[20] X. Liu, C. Zou, Y. Du, and F. Xiao, "A linear consequent pole stator permanent magnet Vernier machine," in *Proc. 17th Int. Conf. Electr. Machines Syst. (ICEMS)*, Hangzhou, China, Oct. 2014, pp. 1753–1756.
[21] X. Zhao and S. Niu, "Design of a novel parallel-hybrid-excited Vernier reluctance machine with improved utilization of redundant winding harmonics," *IEEE Trans. Ind. Electron.*, vol. 65, no. 11, pp. 9056–9067, Nov. 2018.
[22] A. Ishizaki, T. Tanaka, K. Takasaki, and S. Nishikata, "Theory and optimum design of PM Vernier motor," in *Proc. 7th Int. Conf. Electr. Mach. Drives*, Durham, U.K., Sep. 1995, pp. 208–212.
[23] D. K. Jang and J. H. Chang, "Design of a Vernier machine with PM on both sides of rotor and stator," *IEEE Trans. Magn.*, vol. 50, no. 2, pp. 877–880, Feb. 2014.
[24] X. Zhao, S. Niu, and W. Fu, "Design of a novel parallel-hybrid-excited dual-PM machine based on armature harmonics diversity for electric vehicle propulsion," *IEEE Trans. Ind. Electron.*, vol. 66, no. 6, pp. 4209–4219, Jun. 2019.
[25] Q. Wang, S. Niu, and X. Luo, "A novel hybrid dual-PM machine excited by AC with DC bias for electric vehicle propulsion," *IEEE Trans. Ind. Electron.*, vol. 64, no. 9, pp. 6908–6919, Sep. 2017.
[26] X. Zhao, S. Niu, and W. Fu, "Torque component quantification and design guideline for dual permanent magnet Vernier machine," *IEEE Trans. Magn.*, vol. 55, no. 6, Jun. 2019, Art. no. 8101905.
[27] G. Lei, T. Wang, J. Zhu, Y. Guo, and S. Wang, "System-level design optimization method for electrical drive systems-robust approach," *IEEE Trans. Ind. Electron.*, vol. 62, no. 8, pp. 4702–4713, Aug. 2015.
[28] X. Sun, Z. Shi, G. Lei, Y. Guo, and J. Zhu, "Analysis, design and optimization of a permanent magnet synchronous motor for a campus patrol electric vehicle," *IEEE Trans. Veh. Technol.*, to be published.
[29] Z. Shi, X. Sun, Y. Cai, Z. Yang, G. Lei, Y. Guo, and J. Zhu, "Torque analysis and dynamic performance improvement of a PMSM for EVs by skew angle optimization," *IEEE Trans. Appl. Supercond.*, vol. 29, no. 2, pp. 1–5, Mar. 2019.
[30] X. Sun, C. Hu, G. Lei, Y. Guo, and J. Zhu, "State feedback control for a PM hub motor based on grey wolf optimization algorithm," *IEEE Trans. Power Electron.*, to be published.

SHUANGXIA NIU received the B.Sc. and M.Sc. degrees in electrical engineering from Tianjin University, China, in 2002 and 2005, respectively, and the Ph.D. degree from The University of Hong Kong, Hong Kong, in 2009. She is currently an Associate Professor with the Department of Electrical Engineering, The Hong Kong Polytechnic University, Hong Kong. Her research interests include electrical machines and renewable energy conversion.

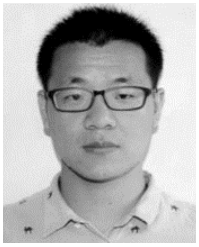

TIANTIAN SHENG received the B.S. and M.S. degrees from the Nanjing University of Aeronautics and Astronautics, Nanjing, China, in 2012 and 2015, respectively. He is currently pursuing the Ph.D. degree with Electrical Engineering Department, The Hong Kong Polytechnic University, Hong Kong. His research interests include stator-PM electric machine, and reluctance machine design and drive.

XING ZHAO received the B.Sc. degree in electrical engineering from the Department of Automation, Nanjing University of Aeronautics and Astronautics, Nanjing, China, in 2014. He is currently pursuing the Ph.D. degree in electrical engineering with the Department of Electrical Engineering, The Hong Kong Polytechnic University, Hong Kong. His research interests include novel electrical machines and drives.

XIAODONG ZHANG received the B.Eng. and M.Eng. degrees from the Department of Automation, Tianjin University, China, in 2002 and 2005, respectively, and the Ph.D. degree in electrical engineering from the Department of Electrical and Electronic Engineering, The University of Hong Kong, Hong Kong, in 2011. His research interest includes electric machine design and control.